International Journal of Solids and Structures 96 (2016) 288–299

Contents lists available at ScienceDirect

International Journal of Solids and Structures

journal homepage: www.elsevier.com/locate/ijsolstr

A finite element framework for distortion gradient plasticity with applications to bending of thin foils

Emilio Martínez-Pañeda[a,*], Christian F. Niordson[b], Lorenzo Bardella[c]

[a] Department of Construction and Manufacturing Engineering, University of Oviedo, Gijón 33203, Spain
[b] Department of Mechanical Engineering, Solid Mechanics, Technical University of Denmark, DK-2800 Kgs. Lyngby, Denmark
[c] Department of Civil, Environmental, Architectural Engineering and Mathematics, University of Brescia, Via Branze, 43, 25123 Brescia, Italy

ARTICLE INFO

Article history:
Received 17 February 2016
Revised 9 May 2016
Available online 2 June 2016

Keywords:
Distortion gradient plasticity
Finite element method
Plastic spin
Energetic and dissipative higher-order stresses
Micro-bending

ABSTRACT

A novel general purpose Finite Element framework is presented to study small-scale metal plasticity. A distinct feature of the adopted *distortion* gradient plasticity formulation, with respect to *strain* gradient plasticity theories, is the constitutive inclusion of the plastic spin, as proposed by Gurtin (2004) through the prescription of a free energy dependent on Nye's dislocation density tensor. The proposed numerical scheme is developed by following and extending the mathematical principles established by Fleck and Willis (2009). The modeling of thin metallic foils under bending reveals a significant influence of the plastic shear strain and spin due to a mechanism associated with the higher-order boundary conditions allowing dislocations to exit the body. This mechanism leads to an unexpected mechanical response in terms of bending moment versus curvature, dependent on the foil length, if either viscoplasticity or isotropic hardening are included in the model. In order to study the effect of dissipative higher-order stresses, the mechanical response under non-proportional loading is also investigated.

1. Introduction

Experiments have shown that metallic materials display strong size effects at both micron and sub-micron scales (Fleck et al., 1994; Nix and Gao, 1998; Stölken and Evans, 1998; Moreau et al., 2005). Much research has been devoted to modeling the experimentally observed change in the material response with diminishing size (Fleck and Hutchinson, 1997; Qu et al., 2006; Klusemann et al., 2013) in addition to studies of size effects in void growth (Liu et al., 2005; Niordson, 2007), fiber reinforced materials (Bittencourt et al., 2003; Niordson, 2003; Legarth and Niordson, 2010), and fracture problems (Martínez-Pañeda and Betegón, 2015; Martínez-Pañeda and Niordson, 2016). Most attempts to model size effects in metals have been based on higher-order continuum modeling, and different theories, both phenomenological (Fleck and Hutchinson, 2001; Gudmundson, 2004; Gurtin, 2004; Gurtin and Anand, 2005) and mechanism-based (Gao et al., 1999) have been developed. All these theories aim at predicting size effects in polycrystalline metals in an average sense, without explicitly accounting for the crystal lattice, nor for the behavior of internal grain boundaries.

While higher-order energetic and dissipative contributions are a common feature among the majority of the most advanced phenomenological Strain Gradient Plasticity (SGP) theories (see, e.g., Gudmundson, 2004; Gurtin and Anand, 2005; 2009; Fleck and Willis, 2009b), the need to constitutively account for the plastic spin, as proposed about ten years ago by Gurtin (2004), to properly describe the plastic flow incompatibility and associated dislocation densities, has been mostly neglected in favor of simpler models. However, the use of phenomenological higher-order formulations that involve the whole plastic distortion (here referred to as *Distortion Gradient Plasticity*, DGP) has attracted increasing attention in recent years due to its superior modeling capabilities. The studies of Bardella and Giacomini (2008) and Bardella (2009; 2010) have shown that, even for small strains, the contribution of the plastic spin plays a fundamental role in order to provide a description closer to the mechanical response prediction of strain gradient *crystal* plasticity. This has been further assessed by Poh and Peerlings (2016), who, by comparing to a reference crystal plasticity solution obtained with the theory by Gurtin and Needleman (2005), showed that the plastic rotation must be incorporated to capture the essential features of crystal plasticity. Moreover, Poh and Peerlings (2016) numerically elucidated that the localization phenomenon taking place in the Bittencourt et al. (2003) composite unit cell benchmark problem can only be reproduced by DGP. Gurtin (2004) theory has also been employed by Poh and

* Corresponding author. Tel: +34699765542; fax: +34 985 18 24 33.
E-mail address: mail@empaneda.com (E. Martínez-Pañeda).

http://dx.doi.org/10.1016/j.ijsolstr.2016.06.001
0020-7683/

co-workers (Poh, 2013; Poh and Phan, 2016) through a novel homogenization formulation to describe the behavior of each grain in a polycrystal where grain boundaries are modeled to describe effects of dislocation blockage or transmittal.

However, despite the superior modeling capability of DGP with respect to SGP, the literature is scarce on the development of a general purpose Finite Element (FE) framework for DGP. Particularly, the use of higher-order dissipative terms - associated with strengthening mechanisms - is generally avoided due to the related computational complexities. This is the case of the very recent FE implementation of Poh and Peerlings (2016) and the earlier work by Ostien and Garikipati (2008), who implemented Gurtin (2004) theory within a Discontinuous Galerkin framework. Energetic and dissipative contributions are both accounted for in the recent *ad hoc* FE formulation for the torsion problem by Bardella and Panteghini (2015), also showing that, contrary to higher-order SGP theories, Gurtin (2004) DGP can predict some energetic strengthening even with a quadratic defect energy.

In this work, a general purpose FE framework for DGP is developed on the basis of an extension of the minimum principles proposed by Fleck and Willis (2009b). The numerical scheme includes both energetic and dissipative higher-order stresses and the effect of the latter under non-proportional loading is investigated. The novel FE framework is particularized to the plane strain case and applied to the bending of thin foils, of particular interest to the study of size effects in metals (see, e.g., Yefimov et al., 2004; Yefimov and Giessen, 2005; Engelen et al., 2006; Evans and Hutchinson, 2009; Idiart et al., 2009; Polizzotto, 2011) since the experiments of Stölken and Evans (1998) (see also Moreau et al., 2005). Computations reveal a dependence of the results on the foil length if either rate-dependent plasticity or isotropic hardening are included in the model. This is a consequence of the definition of the energetic higher-order contribution as a function of Nye's dislocation density tensor (Nye, 1953; Fleck and Hutchinson, 1997; Arsenlis and Parks, 1999), that is intrinsic to Gurtin (2004) theory. This unexpected effect, absent in conventional theories and in many GP theories, is accompanied with the development of plastic shear and plastic spin, which turn out to influence the overall mechanical response in bending. Such a behavior is triggered by the interaction between the conventional and the higher-order boundary conditions, the latter allowing dislocations to exit the foil at the free boundaries. The foil length dependence of the mechanical response is emphasized by the presence of the plastic spin in Gurtin (2004) DGP, but it also characterizes the Gurtin and Anand (2005) SGP theory, still involving Nye's tensor restricted to the assumption of irrotational plastic flow (that is, vanishing plastic spin). Hence, one of the results of the present investigation concerns with the usefulness of two-dimensional analyses with appropriate boundary conditions to model micro-bending phenomenologically.

Outline of the paper. The DGP theory of Gurtin (2004) is presented in Section 2, together with the novel minimum principles governing it. The FE formulation and its validation are described in Section 3. Results concerning bending of thin foils are presented and discussed in Section 4. Some concluding remarks are offered in Section 5.

Notation. We use lightface letters for scalars. Bold face is used for first-, second-, and third-order tensors, in most cases respectively represented by small Latin, small Greek, and capital Latin letters. When we make use of indices they refer to a Cartesian coordinate system. The symbol " $\cdot$ " represents the inner product of vectors and tensors (e.g., $a = \boldsymbol{b}\cdot\boldsymbol{u} \equiv b_i u_i$, $b = \boldsymbol{\sigma}\cdot\boldsymbol{\varepsilon} \equiv \sigma_{ij}\varepsilon_{ij}$, $c = \boldsymbol{T}\cdot\boldsymbol{S} \equiv T_{ijk}S_{ijk}$). For any tensor, say $\boldsymbol{\rho}$, the inner product by itself is $|\boldsymbol{\rho}|^2 \equiv \boldsymbol{\rho}\cdot\boldsymbol{\rho}$. The symbol " $\times$ " is adopted for the vector product: $\boldsymbol{t} = \boldsymbol{m}\times\boldsymbol{n} \equiv e_{ijk}m_j n_k = t_i$, with e_{ijk} denoting the alternating symbol (one of the exceptions, as it is a third-order tensor represented by a small Latin letter), and, for $\boldsymbol{\zeta}$ a second-order tensor: $\boldsymbol{\zeta}\times\boldsymbol{n} \equiv e_{jlk}\zeta_{il}n_k$. For the products of tensors of different order the lower-order tensor is on the right and all its indices are saturated, e.g.: for $\boldsymbol{\sigma}$ a second-order tensor and $\boldsymbol{n}$ a vector, $\boldsymbol{t} = \boldsymbol{\sigma n} \equiv \sigma_{ij}n_j = t_i$; for $\boldsymbol{T}$ a third-order tensor and $\boldsymbol{n}$ a vector, $\boldsymbol{Tn} \equiv T_{ijk}n_k$; for $\mathbb{L}$ a fourth-order tensor and $\boldsymbol{\varepsilon}$ a second-order tensor, $\boldsymbol{\sigma} = \mathbb{L}\boldsymbol{\varepsilon} \equiv L_{ijkl}\varepsilon_{kl} = \sigma_{ij}$. Moreover, $(\nabla\boldsymbol{u})_{ij} \equiv \partial u_i/\partial x_j \equiv u_{i,j}$, $(\mathrm{div}\,\boldsymbol{\sigma})_i \equiv \sigma_{ij,j}$, and $(\mathrm{curl}\,\boldsymbol{\gamma})_{ij} \equiv e_{jkl}\gamma_{il,k}$ designate, respectively, the gradient of the vector field $\boldsymbol{u}$, the divergence of the second-order tensor $\boldsymbol{\sigma}$, and the curl of the second-order tensor $\boldsymbol{\gamma}$, whereas $(\mathrm{dev}\,\boldsymbol{\varsigma})_{ij} \equiv (\varsigma_{ij} - \delta_{ij}\varsigma_{kk}/3)$ (with δ_{ij} the Kronecker symbol), $(\mathrm{sym}\,\boldsymbol{\varsigma})_{ij} \equiv (\varsigma_{ij} + \varsigma_{ji})/2$, and $(\mathrm{skw}\,\boldsymbol{\varsigma})_{ij} \equiv (\varsigma_{ij} - \varsigma_{ji})/2$ denote, respectively, the deviatoric, symmetric, and skew-symmetric parts of the second-order tensor $\boldsymbol{\varsigma}$.

2. The flow theory of distortion gradient plasticity and the new stationarity principles

The theory presented in this section refers to the mechanical response of a body occupying a space region Ω, whose external surface S, of outward normal $\mathbf{n}$, consists of two couples of *complementary* parts: the first couple consists of S_t, where the conventional tractions $\mathbf{t}^0$ are known, and S_u, where the displacement $\mathbf{u}^0$ is known, whereas the second couple consists of S_t^{dis}, where *dislocations are free to exit the body*, and S_u^{dis}, where *dislocations are blocked and may pile-up*: $S = S_t \cup S_u = S_t^{\mathrm{dis}} \cup S_u^{\mathrm{dis}}$.

This section is devoted to the presentation of compatibility, balance, and constitutive equations. For their derivation and for more insight on their mechanical meaning, the reader is referred to Gurtin (2004) and Bardella (2010). Furthermore, we will also provide two minimum principles extending those formulated by Fleck and Willis (2009b) for a higher-order SGP, to Gurtin (2004) DGP. On the basis of these minimum principles we will develop the new FE framework in Section 3.

2.1. Kinematic and static field equations

2.1.1. Compatibility equations

In the small strains and rotations regime, the plastic distortion $\boldsymbol{\gamma}$, that is the plastic part of the displacement gradient, is related to the displacement $\mathbf{u}$ by

$$\nabla\mathbf{u} = (\nabla\mathbf{u})_{\mathrm{el}} + \boldsymbol{\gamma} \quad \text{in} \quad \Omega \tag{1}$$

in which $(\nabla\mathbf{u})_{\mathrm{el}}$ is the elastic part of the displacement gradient. The displacement field $\mathbf{u}$ is assumed to be sufficiently smooth, such that $\mathrm{curl}\nabla\mathbf{u} = \mathbf{0}$ in Ω, and the plastic deformation is assumed to be isochoric, so that $\mathrm{tr}\boldsymbol{\gamma} = 0$. The total strain, Nye's dislocation density tensor (Nye, 1953; Fleck and Hutchinson, 1997; Arsenlis and Parks, 1999), the plastic strain, and the plastic spin are, respectively, defined as:

$$\boldsymbol{\varepsilon} = \mathrm{sym}\nabla\mathbf{u}, \quad \boldsymbol{\alpha} = \mathrm{curl}\boldsymbol{\gamma}, \quad \boldsymbol{\varepsilon}^p = \mathrm{sym}\boldsymbol{\gamma}, \quad \boldsymbol{\vartheta}^p = \mathrm{skw}\boldsymbol{\gamma} \quad \text{in} \quad \Omega \tag{2}$$

2.1.2. Balance equations

For the whole body free from standard body forces, the conventional balance equation reads

$$\mathrm{div}\boldsymbol{\sigma} = \mathbf{0} \quad \text{in} \quad \Omega \tag{3}$$

with $\boldsymbol{\sigma}$ denoting the standard symmetric Cauchy stress.

The higher-order balance equation can be conveniently written into its symmetric and skew-symmetric parts:

$$\boldsymbol{\rho} - \mathrm{dev}\boldsymbol{\sigma} - \mathrm{div}\mathbf{T}^{(\varepsilon)} + \mathrm{sym}[\mathrm{dev}(\mathrm{curl}\boldsymbol{\zeta})] = \mathbf{0} \quad \text{in} \quad \Omega \tag{4}$$

$$\boldsymbol{\omega} + \mathrm{skw}(\mathrm{curl}\boldsymbol{\zeta}) = \mathbf{0} \quad \text{in} \quad \Omega \tag{5}$$

in which $\boldsymbol{\rho}$, $\boldsymbol{\omega}$, and $\mathbf{T}^{(\varepsilon)}$ are the dissipative stresses constitutively conjugate to the plastic strain rate $\dot{\boldsymbol{\varepsilon}}^p$, the plastic spin rate $\dot{\boldsymbol{\vartheta}}^p$, and the gradient of the plastic strain rate $\nabla\dot{\boldsymbol{\varepsilon}}^p$, respectively, whereas $\boldsymbol{\zeta}$ is the energetic stress (called defect stress) constitutively conjugate to Nye's tensor $\boldsymbol{\alpha}$.

Note that $\boldsymbol{\rho}$ and $\boldsymbol{\omega}$ can be summed up to obtain a dissipative stress, $\boldsymbol{\varsigma}$, conjugate to the plastic distortion rate $\dot{\boldsymbol{\gamma}}$:

$$\boldsymbol{\varsigma} = \boldsymbol{\rho} + \boldsymbol{\omega} \quad \text{such that} \quad \boldsymbol{\rho} = \mathrm{sym}\boldsymbol{\varsigma}, \quad \boldsymbol{\omega} = \mathrm{skw}\boldsymbol{\varsigma}, \quad \mathrm{tr}\boldsymbol{\varsigma} = 0 \tag{6}$$

2.2. Boundary conditions

2.2.1. Kinematic boundary conditions

The conventional kinematic boundary conditions are:

$$\dot{\mathbf{u}} = \dot{\mathbf{u}}^0 \quad \text{on } S_u \tag{7}$$

whereas we adopt homogeneous higher-order kinematic (essential) boundary conditions, which are called microhard boundary conditions as they describe dislocations piling up at the boundary. If the complete DGP theory - including the third-order dissipative stress $\mathbf{T}^{(\varepsilon)}$ - is considered, the microhard boundary conditions read:

$$\dot{\boldsymbol{\varepsilon}}^p = \mathbf{0} \quad \text{and} \quad \dot{\boldsymbol{\vartheta}}^p \times \mathbf{n} = \mathbf{0} \quad \text{on } S_u^{\mathrm{dis}} \tag{8}$$

Otherwise, in the simpler DGP theory neglecting $\mathbf{T}^{(\varepsilon)}$, the microhard boundary conditions read:

$$\dot{\boldsymbol{\gamma}} \times \mathbf{n} = \mathbf{0} \quad \text{on } S_u^{\mathrm{dis}} \tag{9}$$

2.2.2. Static boundary conditions

The conventional static boundary conditions are:

$$\boldsymbol{\sigma}\mathbf{n} = \mathbf{t}^0 \quad \text{on} \quad S_t \tag{10}$$

whereas we adopt homogeneous higher-order static (natural) boundary conditions, which are called microfree boundary conditions as they describe dislocations free to exit the body:

$$\mathbf{T}^{(\varepsilon)}\mathbf{n} + \mathrm{sym}[\mathrm{dev}(\boldsymbol{\zeta} \times \mathbf{n})] = \mathbf{0} \quad \text{on} \quad S_t^{\mathrm{dis}} \tag{11}$$

$$\mathrm{skw}(\boldsymbol{\zeta} \times \mathbf{n}) = \mathbf{0} \quad \text{on} \quad S_t^{\mathrm{dis}} \tag{12}$$

2.3. Stationarity principles

In the literature, one of the most common ways to obtain a weak form of the balance equations, useful for the numerical implementation, is based on the Principle of Virtual Work (PVW, see, e.g., Fleck and Hutchinson, 2001; Gudmundson, 2004; Gurtin, 2004). Here, inspired by the work of Fleck and Willis (2009a; 2009b), we instead provide two stationarity principles, leading to the foregoing balance equations, which result in *minimum* principles after appropriate constitutive choices are made. For a given Cauchy stress, the higher-order balance Eqs. (4) and (5) and homogeneous boundary conditions are satisfied by any suitably smooth field $\dot{\boldsymbol{\gamma}}$ such that the following functional attains stationarity

$$\mathcal{H}_1(\dot{\boldsymbol{\gamma}}) = \int_\Omega \left[\boldsymbol{\rho}\cdot\dot{\boldsymbol{\varepsilon}}^p + \boldsymbol{\omega}\cdot\dot{\boldsymbol{\vartheta}}^p + \mathbf{T}^{(\varepsilon)}\cdot\nabla\dot{\boldsymbol{\varepsilon}}^p + \boldsymbol{\zeta}\cdot\dot{\boldsymbol{\alpha}} - \boldsymbol{\sigma}\cdot\dot{\boldsymbol{\varepsilon}}^p\right]\mathrm{d}V \tag{13}$$

subject to the kinematic relations (2).

For a given plastic strain rate, the conventional balance equation (3) and static boundary condition (10) are satisfied by any kinematically admissible field $\dot{\mathbf{u}}$ that minimizes the following functional:

$$\mathcal{J}(\dot{\boldsymbol{u}}) = \frac{1}{2}\int_\Omega \mathbb{L}\left(\mathrm{sym}\nabla\dot{\mathbf{u}} - \dot{\boldsymbol{\varepsilon}}^p\right)\cdot\left(\mathrm{sym}\nabla\dot{\mathbf{u}} - \dot{\boldsymbol{\varepsilon}}^p\right)\mathrm{d}V - \int_{S_t}\dot{\mathbf{t}}^0\cdot\dot{\boldsymbol{u}}\ \mathrm{d}A \tag{14}$$

Here $\mathbb{L}$ is the elastic stiffness, relating the elastic strain to the Cauchy stress, $\boldsymbol{\sigma} = \mathbb{L}(\boldsymbol{\varepsilon} - \boldsymbol{\varepsilon}^p)$.

2.4. Constitutive laws for the energetic terms (recoverable stresses)

In order to account for the influence of geometrically necessary dislocations (GNDs, see, e.g., Ashby, 1970; Fleck et al., 1994; Fleck and Hutchinson, 1997), the free energy is chosen by Gurtin (2004) to depend on both the elastic strain, $\boldsymbol{\varepsilon} - \boldsymbol{\varepsilon}^p$, and Nye's tensor $\boldsymbol{\alpha}$:

$$\Psi = \frac{1}{2}\mathbb{L}(\boldsymbol{\varepsilon} - \boldsymbol{\varepsilon}^p)\cdot(\boldsymbol{\varepsilon} - \boldsymbol{\varepsilon}^p) + \mathscr{D}(\boldsymbol{\alpha}) \tag{15}$$

in which $\mathscr{D}(\boldsymbol{\alpha})$ is the so-called *defect energy*, accounting for the plastic distortion incompatibility. The recoverable mechanisms associated with development of GNDs are incorporated in the current higher-order theory by assuming the following quadratic defect energy:

$$\mathscr{D}(\boldsymbol{\alpha}) = \frac{1}{2}\mu\ell^2\boldsymbol{\alpha}\cdot\boldsymbol{\alpha} \tag{16}$$

in which μ is the shear modulus and ℓ is an energetic length scale. Hence, the defect stress reads:

$$\boldsymbol{\zeta} = \frac{\partial\mathscr{D}(\boldsymbol{\alpha})}{\partial\boldsymbol{\alpha}} = \mu\ell^2\boldsymbol{\alpha} \tag{17}$$

It has been recently shown by Bardella and Panteghini (2015) that it may be convenient to express the defect energy in terms of more invariants of $\boldsymbol{\alpha}$, as originally envisaged by Gurtin (2004). It may also be relevant to adopt less-than-quadratic forms of the defect energy (e.g., Ohno and Okumura, 2007; Bardella, 2010; Garroni et al., 2010; Forest and Guéninchault, 2013; Bardella and Panteghini, 2015), or even non-convex forms (e.g., Lancioni et al., 2015 and references therein). However, the quadratic defect energy is perfectly suitable for the scope of the present investigation, that is implementing Gurtin (2004) DGP theory in a general purpose FE framework and bringing new features of its predictive capabilities to attention by analyzing the bending of thin foils. We leave for further investigations the analysis of other forms of the defect energy.

2.5. Constitutive laws for the dissipative terms (unrecoverable stresses)

The unrecoverable stresses are prescribed in the form:

$$\boldsymbol{\rho} = \frac{2}{3}\frac{\Sigma}{\dot{E}^p}\dot{\boldsymbol{\varepsilon}}^p, \qquad \boldsymbol{\omega} = \chi\frac{\Sigma}{\dot{E}^p}\dot{\boldsymbol{\vartheta}}^p, \qquad \boldsymbol{T}^{(\varepsilon)} = \frac{2}{3}L^2\frac{\Sigma}{\dot{E}^p}\nabla\dot{\boldsymbol{\varepsilon}}^p \tag{18}$$

where the following phenomenological effective plastic flow rate

$$\dot{E}^p = \sqrt{\frac{2}{3}|\dot{\boldsymbol{\varepsilon}}^p|^2 + \chi|\dot{\boldsymbol{\vartheta}}^p|^2 + \frac{2}{3}L^2|\nabla\dot{\boldsymbol{\varepsilon}}^p|^2} \tag{19}$$

is work conjugate to the effective flow resistance:

$$\Sigma = \sqrt{\frac{3}{2}|\boldsymbol{\rho}|^2 + \frac{1}{\chi}|\boldsymbol{\omega}|^2 + \frac{3}{2L^2}|\boldsymbol{T}^{(\varepsilon)}|^2} \tag{20}$$

such that the 2nd law of thermodynamics is satisfied:

$$\boldsymbol{\rho}\cdot\dot{\boldsymbol{\varepsilon}}^p + \boldsymbol{\omega}\cdot\dot{\boldsymbol{\vartheta}}^p + \mathbf{T}^{\varepsilon}\cdot\nabla\dot{\boldsymbol{\varepsilon}}^p \equiv \Sigma\dot{E}^p > 0 \quad \forall \quad \dot{\boldsymbol{\gamma}} \neq \mathbf{0} \tag{21}$$

In the constitutive laws above L is a dissipative material length parameter and χ is the material parameter governing the dissipation due to the plastic spin[1].

The form of the function $\Sigma(\dot{E}^p, E^p)$, whose dependence on E^p may describe higher-order isotropic hardening, has to be appropriately chosen to complete the set of constitutive prescriptions for the unrecoverable stresses.

With these constitutive equations plastic dissipation may be derived from the dissipation potential

$$\mathscr{V}(\dot{E}^p, E^p) = \int_0^{\dot{E}^p} \Sigma(e, E^p)\mathrm{d}e \tag{22}$$

which is assumed to be convex in $\dot{E}^p$. This is important for the development of a numerical solution procedure, as it makes the stationarity principle based on functional (13) a *minimum* principle, whose functional reads:

$$\mathcal{H}(\dot{\boldsymbol{\gamma}}) = \int_\Omega \left[\mathscr{V}(\dot{E}^p, E^p) + \boldsymbol{\zeta}\cdot\dot{\boldsymbol{\alpha}} - \boldsymbol{\sigma}\cdot\dot{\boldsymbol{\varepsilon}}^p\right]\mathrm{d}V \tag{23}$$

Note that in functional (23) $\dot{E}^p$ is a function of $\dot{\boldsymbol{\gamma}}$ through equation (19) and the kinematic relations (2).

Minimum principles (14) and (23) extend the analogous principles of Fleck and Willis (2009b) to the DGP theory of Gurtin (2004).

In this work we choose the following viscoplastic potential

$$\mathscr{V}(\dot{E}^p, E^p) = \frac{\sigma_Y(E^p)\dot{\varepsilon}_0}{m+1}\left(\frac{\dot{E}^p}{\dot{\varepsilon}_0}\right)^{m+1} \tag{24}$$

so that

$$\Sigma(\dot{E}^p, E^p) = \sigma_Y(E^p)\left(\frac{\dot{E}^p}{\dot{\varepsilon}_0}\right)^{m} \tag{25}$$

with m denoting the rate sensitivity exponent, $\sigma_Y(E^p)$ the current flow stress given by the hardening rule, and $\dot{\varepsilon}_0$ the reference strain rate.

3. Finite element formulation

The present FE framework is based on the minimum principles (14) and (23). General FE implementations of viscoplastic dissipative strain gradient plasticity based on the PVW (e.g., Fredriksson and Gudmundson, 2005; Borg et al., 2006; Niordson and Legarth, 2010) solve for the time derivative of the plastic rate field. The main advantage of employing the minimum principles adopted in the present paper is that the plastic distortion rate field is directly obtained from (23) in the context of dissipative gradient effects. This makes the present numerical scheme more robust as it allows for larger time increments and it enables convergence for lower values of the rate sensitivity exponent. Largely, time-independent behavior may be obtained for sufficiently small rate sensitivity exponents, circumventing complications in the corresponding time-independent model associated with identifying active plastic zones (by, for instance, using image analysis, as proposed by Nielsen and Niordson, 2014). Stationarity of (23) together with the constitutive equations (18) results in the following equation

$$\int_\Omega \left[\frac{2}{3}\frac{\Sigma}{\dot{E}^p}\dot{\boldsymbol{\varepsilon}}^p\cdot\delta\dot{\boldsymbol{\varepsilon}}^p + \chi\frac{\Sigma}{\dot{E}^p}\dot{\boldsymbol{\vartheta}}^p\cdot\delta\dot{\boldsymbol{\vartheta}}^p + \frac{2}{3}L^2\frac{\Sigma}{\dot{E}^p}\nabla\dot{\boldsymbol{\varepsilon}}^p\cdot\delta\nabla\dot{\boldsymbol{\varepsilon}}^p\right]\mathrm{d}V = \int_\Omega\left[\boldsymbol{\sigma}\cdot\delta\dot{\boldsymbol{\varepsilon}}^p - \boldsymbol{\zeta}\cdot\delta\dot{\boldsymbol{\alpha}}\right]\mathrm{d}V \tag{26}$$

Given the recoverable stresses, fulfillment of the above weak form (26) of the higher-order equilibrium equations (4) and (5) directly delivers the plastic distortion rate field, $\dot{\boldsymbol{\gamma}}$. Adopting Voigt notation, the following FE interpolation is used:

$$\dot{\boldsymbol{u}} = \sum_{n=1}^{N_I}\boldsymbol{N}^{(n)}\dot{a}^{(n)} \tag{27}$$

$$\dot{\boldsymbol{\gamma}} = \sum_{n=1}^{N_{II}}\boldsymbol{M}^{(n)}\dot{\gamma}^{(n)} \tag{28}$$

Here $\dot{a}^{(n)} = [\dot{a}_1^{(n)}, \dot{a}_2^{(n)}]^T$ and $\dot{\gamma}^{(n)} = [\dot{\gamma}_{11}^{(n)},\ \dot{\gamma}_{22}^{(n)},\ \dot{\gamma}_{12}^{(n)},\ \dot{\gamma}_{21}^{(n)}]^T$ are nodal degrees of freedom and N_I and N_{II} are the number of nodes employed for the displacement and the plastic distortion interpolations, respectively. Quadratic shape functions are used for the displacement field ($N_I = 8$) while linear shape functions are employed for the plastic distortion field ($N_{II} = 4$).

Let us note that the continuity requirements for the shape functions related to the unconventional FE degrees of freedom are dictated by the structure of the kinematic higher-order boundary conditions, specified in Section 2.2.1. Hence, it is important to point out that we always consider a non-zero dissipative length scale L, whereas we set it to a very small positive number when we want to suppress the effect of the higher-order dissipation. Therefore, we refer to the higher-order boundary conditions (8), which imply that each plastic strain component must be continuous in the whole domain. This would not be necessarily the case in the theory not accounting for dissipative higher-order stresses ($L = 0$ in definition (19)), in which the shape functions for the unconventional FE degrees of freedom should be established on the basis of the structure of the boundary conditions (9). For what concerns the plastic spin, in the plane strain framework considered in this work there is one single component, so that conditions (8) still imply that this component must be continuous in the whole domain. Overall, the foregoing discussion implies that the four plastic distortion components, adopted as unconventional nodal degrees of freedom as specified in Eq. (28), should be approximated by continuous shape functions.

For general three-dimensional boundary value problems, a totally similar FE framework, in which the eight plastic distortion components are employed as unconventional nodal degrees of freedom and are interpolated by continuous shape functions, can be used by slightly modifying the DGP theory. One should extend the effective plastic flow rate definition (19) by including the gradient of the plastic spin rate, weighed by a new dissipative length scale, say L_ϑ. Of course, with such an extension the DGP theory would be enriched by a further dissipative third-order stress, having nine components, whose divergence would enter the higher-order balance equation (5). In this case, the microhard boundary conditions would read $\dot{\boldsymbol{\gamma}} = \boldsymbol{0}$ on S_u^{dis}. It is uncertain whether the predictive capability of the DGP modelling would largely benefit from such an extension (as inferred by the preliminary analysis in the appendix of Bardella, 2010), but it would be worth investigating, as it leads to a convenient FE implementation as that studied in the present paper.[2]

[1] By analyzing the simple shear problem, Bardella (2009) has provided an analytical expression suggesting that, in order to represent the mechanical response of a *crystal* subject to multislip, $\chi \in [0, 2/3]$. However, values of χ larger than 2/3 might help in representing the response of crystals in which the plastic flow has preferential orientations.

[2] On the contrary, the Gurtin (2004) DGP theory involving, as higher-order contribution, exclusively the defect energy written in terms of Nye's dislocation density tensor (i.e., $L \equiv 0$ in the theory presented in Section 2) may be more suitably

Let us finally recall that the static higher-order boundary conditions, specified by Eqs. (11) and (12), are microfree, so that there is no higher-order tractions vector to impose on the boundary S_t^{dis}, where leaving unconstrained an unconventional (plastic) degree of freedom is related to the freedom left to dislocations to exit the body. Dually, setting to zero a plastic degree of freedom on the boundary S_u^{dis} may trigger plastic distortion gradients, contributing to the size effect through the stiffening of a boundary layer region.

Upon finite element discretization, the weak form (26) of the equilibrium equations (4) and (5) results in a system which is of homogeneous degree zero in terms of the unknown plastic distortion rate field. Imposing the variational form (26) to hold for any kinematically admissible variation of $\dot{\boldsymbol{\gamma}}$ leads to the following system of equations, here written in the iterative form (with l denoting the iteration number) actually implemented:

$$\int_\Omega \left(\frac{\Sigma}{(\dot{E}^p)_{(l-1)}} \left[\frac{2}{3} \left(\operatorname{sym}\boldsymbol{M}^{(n)}\right) \cdot \left(\operatorname{sym}\boldsymbol{M}^{(m)}\right) + \chi \left(\operatorname{skw}\boldsymbol{M}^{(n)}\right) \cdot \left(\operatorname{skw}\boldsymbol{M}^{(m)}\right) + \frac{2}{3} L^2 \left(\operatorname{sym}\nabla \boldsymbol{M}^{(n)}\right) \cdot \left(\operatorname{sym}\nabla \boldsymbol{M}^{(m)}\right) \right] \right) \mathrm{d}V \cdot \left(\dot{\gamma}^{(m)}\right)_{(l)} = \int_\Omega \left(\boldsymbol{\sigma} \cdot \left(\operatorname{sym}\boldsymbol{M}^{(n)}\right) - \boldsymbol{\zeta} \cdot \left(\operatorname{curl}\boldsymbol{M}^{(n)}\right) \right) \mathrm{d}V \tag{29}$$

Here the operators $\operatorname{sym}\boldsymbol{M}^{(n)}$, $\operatorname{skw}\boldsymbol{M}^{(n)}$, $\operatorname{sym}\nabla\boldsymbol{M}^{(n)}$, and $\operatorname{curl}\boldsymbol{M}^{(n)}$ contain the shape functions which deliver the discretizations of $\dot{\boldsymbol{\varepsilon}}^p$, $\dot{\boldsymbol{\vartheta}}^p$, $\nabla\dot{\boldsymbol{\varepsilon}}^p$, and $\dot{\boldsymbol{\alpha}}$, respectively, from the nodal values of the plastic distortion $\dot{\gamma}^{(n)}$ (see Appendix A). Following Niordson and Hutchinson (2011), the system of equations (29) is solved iteratively for $\dot{\gamma}^{(m)}$ on the basis of the known energetic stresses $(\boldsymbol{\sigma}, \boldsymbol{\zeta})$ for the current state, written in terms of the total displacement $\boldsymbol{u}$ and plastic distortion $\boldsymbol{\gamma}$ fields at the beginning of the time increment. At a general time increment, the plastic distortion rate field from the previous increment is used as a starting guess. Convergence of the iteration is defined when the relative norm of the change in the plastic distortion rate field is below an appropriate threshold value. Finally, the plastic distortion rate $\dot{\boldsymbol{\gamma}}$ is determined from the discretization (28).

Subsequently, for a known plastic distortion rate field, the incremental solution for the displacement is determined by finding the minimum of functional (14). The stationarity ensuing from this second minimum principle corresponds to the conventional virtual work statement and, therefore, its implementation into a FE code is standard. Thus, for the sake of brevity, further details are here omitted. In the present incremental procedure we use a Forward Euler time integration scheme, whereas the above described iterative algorithm is implemented so as to ensure convergence in the computation of the plastic distortion rate field. A time increment sensitivity analysis has been conducted in all computations to ensure that the numerical solution does not drift away from the equilibrium configuration.

3.1. Validation of the FE implementation

In order to validate the present numerical model, the simple shear of a constrained strip is analyzed so as to compare the results with those obtained by Bardella (2010) from the minimization of the Total Complementary Energy functional in the deformation theory context. As in Bardella (2010), we consider a long strip of height H free from body forces, with isotropic behavior and sheared between two bodies in which dislocations cannot penetrate. Hence, the displacement is fully constrained in the lower strip surface, $u_1(x_2 = 0) = u_2(x_2 = 0) = 0$, while the upper strip surface is subjected to uniform horizontal displacement $u_1(x_2 = H) = \Gamma H$ with $u_2(x_2 = H) = 0$. Here, Γ is referred to as the applied strain, whose rate, in the following, is assumed to be equal to the adopted reference strain rate ($\dot{\Gamma} = \dot{\varepsilon}_0$). Since dislocations pile-up when they reach the strip lower and upper surfaces, the plastic distortion must be zero at $x_2 = 0$ and $x_2 = H$. The problem is essentially one-dimensional, so that the strip, unbounded along both the shearing direction x_1 and the x_3 direction, is modeled using a single column of 80 plane strain quadrilateral elements along the strip height (H) with appropriate boundary conditions at the sides of the column ($u_2 = \gamma_{11} = \gamma_{22} = 0\ \forall x_2$).

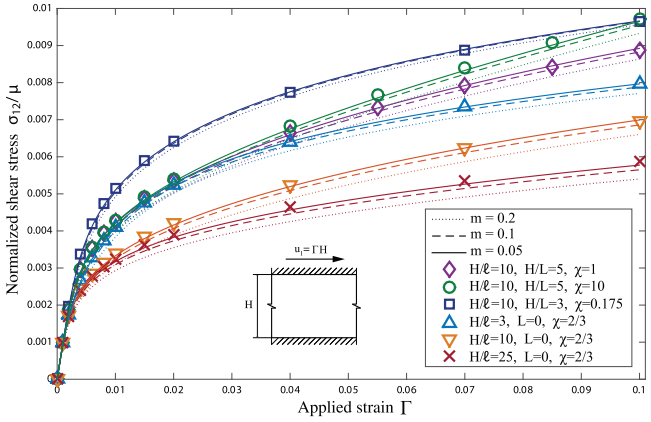

Fig. 1. Simple shear of a constrained strip. Comparison of the numerical results of the present model (lines) with the predictions of Bardella (2010) (symbols) for different values of H/ℓ, H/L, and χ. The case $L = 0$ is numerically approximated by setting $L/H = 0.01$. Other material parameters are $\sigma_0 = 200$ MPa, $\varepsilon_0 = 0.02$, $N = 0.2$, $\mu = 26.3$ GPa, and $\dot{\varepsilon}_0 = 0.02\ \text{s}^{-1}$.

In order to compare our results with those of Bardella (2010), the following hardening law is used:

$$\sigma_Y(E^p) = \sigma_0 \left(\frac{E^p}{\varepsilon_0} \right)^N \tag{30}$$

We consider the following material properties: $\mu = 26.3$ GPa, $\varepsilon_0 = 0.02$, $\sigma_0 = 200$ MPa, and $N = 0.2$.

Within the rate-dependent framework adopted, a reference strain rate of $\dot{\varepsilon}_0 = 0.02\ \text{s}^{-1}$ is assumed and the effect of the viscoplastic exponent m is studied in order to approach rate-independent behavior (see Eq. (25)). Fig. 1 shows the numerical results obtained for different combinations of the material parameter governing the dissipation due to the plastic spin, χ, and the energetic and dissipative length scales, in terms of the ratios H/ℓ and H/L, respectively. Discrete symbols represent the results obtained by Bardella (2010) while solid lines ($m = 0.05$), dashed lines ($m = 0.1$), and dotted lines ($m = 0.2$) show the results of the present FE implementation.

As it can be seen in Fig. 1, the FE framework reproduces the results of Bardella (2010) with a very good qualitative and quantitative agreement[3].

4. Modeling the bending of thin foils

A foil of thickness H and length W subjected to bending is analyzed. As depicted in Fig. 2, illustrating the conventional boundary conditions, we impose the longitudinal displacement component at

implemented by the so-called curl-conforming Nédélec finite elements (Wieners and Wohlmuth, 2011).

[3] Note that the results of Bardella (2010) are not exact as they were obtained numerically by applying the Rayleigh-Ritz method to the Total Complementary Energy functional. Hence, the present analysis also validates the Rayleigh-Ritz discretization adopted by Bardella (2010).

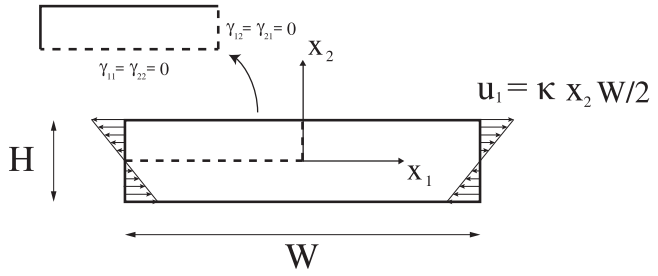

Fig. 2. Bending of thin foil: boundary conditions on the undeformed configuration.

the foil ends:

$$u_1 = x_2 x_1 \kappa \quad \text{at} \quad x_1 \pm W/2 \tag{31}$$

whereas the *complementary* boundary part is traction-free. In Eq. (31), κ is the curvature that the foil would attain if modeled by a conventional theory, henceforth referred to as the *applied curvature*. The higher-order boundary conditions are microfree on the entire boundary. These boundary conditions are adopted for all the monotonic loading analyses. Note that solving the micro-bending problem as a two-dimensional boundary value problem is quite different from what has been done so far in the phenomenological GP literature, in which, usually (see, e.g., Engelen et al., 2006; Evans and Hutchinson, 2009; Idiart et al., 2009; Polizzotto, 2011), the total deformation field is assumed *pointwise* on the basis of the conventional bending theory, thus solving for a plastic strain field independent of x_1. Instead, Yefimov et al. (2004) and Yefimov and Giessen (2005) used a two-dimensional plane strain model to analyze the micro-bending of single crystals by comparing the results of discrete dislocation dynamics with those of a backstress-based strain gradient crystal plasticity theory. In both cases, Yefimov et al. employ the conventional boundary conditions (31) and allow dislocations to exit the foil when they reach its free boundaries, which corresponds to the microfree boundary condition assumed in this work.

As detailed in Section 4.1, the structure of the microfree boundary conditions is the responsible for the need to solve a two-dimensional boundary value problem in order to obtain the solution of the micro-bending problem described by the here concerned Nye's tensor-based phenomenological GP. In particular, we will show that the boundary conditions here adopted lead to a peculiar mechanical response whose validation would require specific experiments. Moreover, our results imply that modeling actual bending experiments available in literature (Stölken and Evans, 1998; Moreau et al., 2005) may require two-dimensional analysis and particular attention to the boundary conditions to be imposed, the latter being not necessarily those used in this study.

By exploiting symmetry and skew-symmetry conditions of the bending problem, we may impose that:

$$\gamma_{11} = \gamma_{22} = 0 \ \text{ at } \ x_2 = 0 \quad \text{and} \quad \gamma_{12} = \gamma_{21} = 0 \ \text{ at } \ x_1 = 0 \tag{32}$$

in such a way as to model only one fourth of the foil, as depicted in Fig. 2. The vertical displacement of the center node is constrained in order to suppress rigid body motion.

4.1. Micro-bending within Nye's tensor-based phenomenological gradient plasticity

In plane strain problems the sole non-vanishing Nye's tensor components are

$$\alpha_{13} = \gamma_{12,1} - \varepsilon^p_{11,2}, \quad \alpha_{23} = \varepsilon^p_{22,1} - \gamma_{21,2}, \quad \alpha_{31} = \varepsilon^p_{33,2}, \quad \alpha_{32} = -\varepsilon^p_{33,1} \tag{33}$$

At the foil ends the homogeneous microfree boundary conditions (11) and (12) provide

$$\frac{2}{3}L^2 \frac{\Sigma}{\dot{E}^p} \dot{\varepsilon}^p_{11,1} + \frac{\mu \ell^2}{3}(\varepsilon^p_{11,1} + \gamma_{21,2}) = 0 \quad \text{at} \quad x_1 = \pm W/2 \tag{34}$$

$$\frac{2}{3}L^2 \frac{\Sigma}{\dot{E}^p} \dot{\varepsilon}^p_{12,1} + \frac{\mu \ell^2}{2}(\gamma_{12,1} - \varepsilon^p_{11,2}) = 0 \quad \text{at} \quad x_1 = \pm W/2 \tag{35}$$

$$\frac{2}{3}L^2 \frac{\Sigma}{\dot{E}^p} \dot{\varepsilon}^p_{22,1} + \frac{\mu \ell^2}{3}(\varepsilon^p_{11,1} + 3\varepsilon^p_{22,1} - 2\gamma_{21,2}) = 0 \quad \text{at} \quad x_1 = \pm W/2 \tag{36}$$

$$\gamma_{12,1} - \varepsilon^p_{11,2} = 0 \quad \text{at} \quad x_1 = \pm W/2 \tag{37}$$

Combination of (35) and (37) leads to

$$\dot{\varepsilon}^p_{12,1} = 0 \quad \text{at} \quad x_1 = \pm W/2 \tag{38}$$

At the foil top and bottom surfaces the microfree boundary conditions (11) and (12) provide similar relations, among which the most relevant reads:

$$\frac{2}{3}L^2 \frac{\Sigma}{\dot{E}^p} \dot{\varepsilon}^p_{11,2} - \frac{\mu \ell^2}{3}(2\gamma_{12,1} - 3\varepsilon^p_{11,2} - \varepsilon^p_{22,2}) = 0 \quad \text{at} \quad x_2 = \pm H/2 \tag{39}$$

Inspection of the foregoing equations, with particular reference to (37), allows us to deduct that, in the plastic regime, at the foil end regions a non-vanishing γ_{12} must develop. Furthermore, when $\varepsilon^p_{11,2}$ becomes sufficiently large, an increase of $\gamma_{12,1}$ is expected in order to minimize the defect energy in the end regions (see Nye's tensor component α_{13} in Eq. (33)). *This implies that, for a given H, the DGP theory here concerned may predict a mechanical response dependent on the foil length W.* Let us notice that the contributions of ϑ^p_{12} and ε^p_{12} to γ_{12} depend on the chosen material parameters. In particular, $\chi = 0$ makes it energetically convenient to develop plastic spin to minimize the defect energy, while $\chi \to \infty$ leads to the irrotational plastic flow condition of Gurtin and Anand (2005), allowing for the development of ε^p_{12} only.

With the aim of gaining insight into the role of both ε^p_{12} and ϑ^p_{12} in the bending problem, we have carried out several analyses with the present FE framework. Unless otherwise specified, the ratio $W/H = 30$ is adopted.

For each case presented different mesh densities were used to ensure achieved convergence. Typically, 20 quadrilateral elements were employed along the thickness and uniform meshes were used, with element aspect ratio equal to 1. Both full- and reduced-integration plane strain elements (having, respectively, nine and four Gauss integration points) were tested and no shear locking effects were observed. For the sake of clarity we will focus our attention to perfectly plastic behavior, that is $N = 0$ in Eq. (30).

Henceforth, we adopt the following material properties: $\mu = 26.3$ GPa, Poisson's ratio $\nu = 0.3$, initial yield stress $\sigma_0 = 200$ MPa, and reference strain rate $\dot{\varepsilon}_0 = 0.02\ \text{s}^{-1}$. Other material parameters will be specified case by case. Unless otherwise stated, the dissipative and energetic length scales are such that

$$H/L = 2.5 \quad \text{and} \quad H/\ell = 5$$

The specimen is loaded at a rate of curvature $\dot{\kappa} = \sqrt{3}\dot{\varepsilon}_0/H$, such that, in conventional bending, the most stretched material points would be loaded at a conventional effective plastic strain rate equal to $\dot{\varepsilon}_0$ when elastic strain increments vanish.

Fig. 3 represents the contours obtained for γ_{12}, ε^p_{12}, and ϑ^p_{12} at the applied normalized curvature $H\kappa/\sqrt{3} = 0.05$. The influence of different values of χ is examined by adopting $\chi = 0.1$, $\chi = 2/3$,

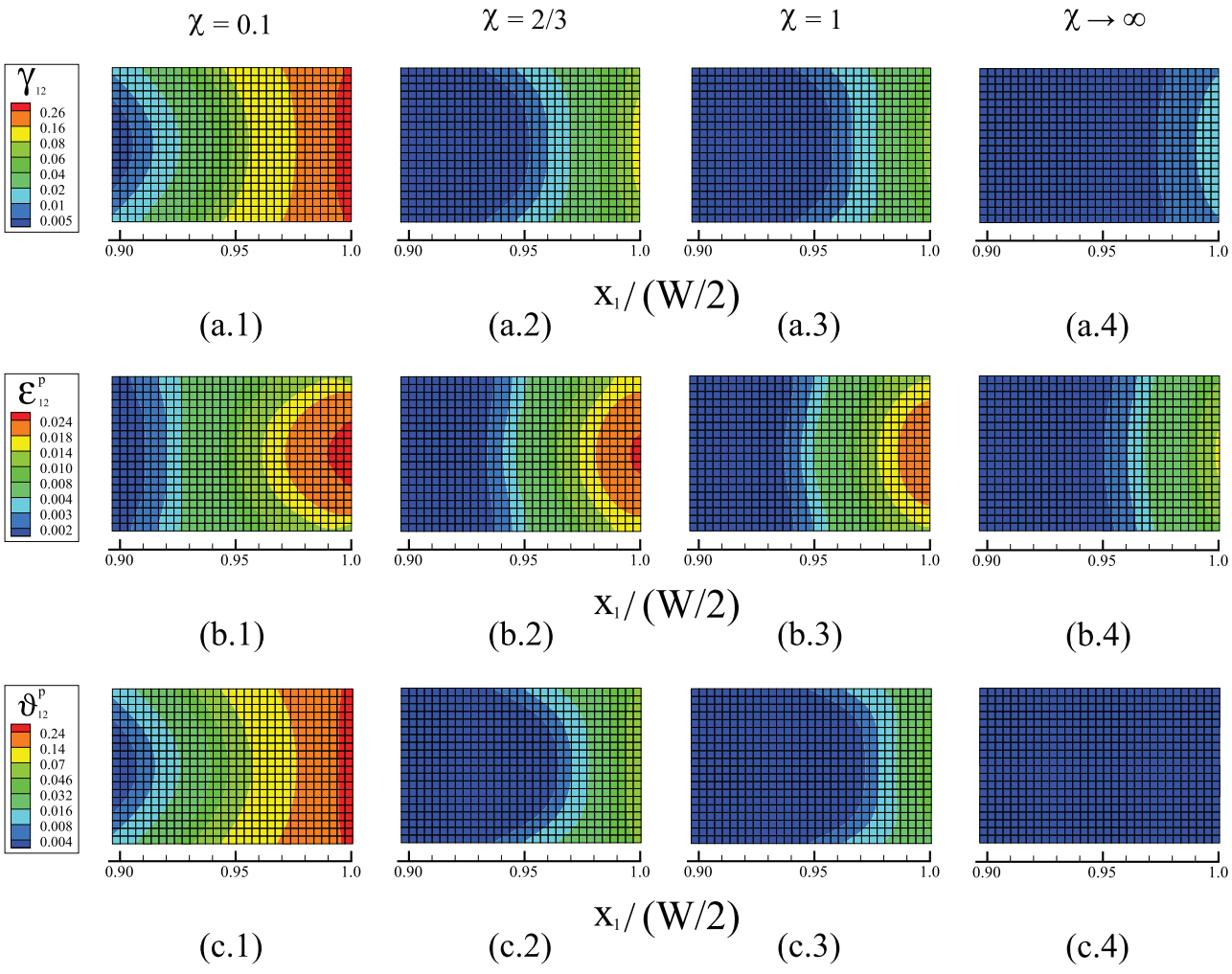

Fig. 3. Contours of γ_{12} (a), ε^p_{12} (b), and ϑ^p_{12} (c) at $H\kappa/\sqrt{3} = 0.05$ for $\chi = 0.1$ (1), 2/3 (2), 1 (3), and $\chi \to \infty$ (4). The rate sensitivity exponent is $m = 0.05$.

$\chi = 1$, and $\chi \to \infty$. $\chi = 2/3$ is an upper limit estimate to represent crystal multislip (Bardella, 2009) and makes the effective plastic flow rate (19) equal to the norm of the plastic distortion in the absence of dissipative higher-order terms. $\chi \to \infty$ reproduces the conditions of Gurtin and Anand (2005) SGP theory.

The results reveal a strong influence of γ_{12} (Fig. 3(a.1)–(a.4)), which increases towards the foil end. Unexpected within a classical framework, both ε^p_{12} (Fig. 3(b.1)–(b.3)) and ϑ^p_{12} (Fig. 3(c.1)–(c.3)) assume relevant values in a significant foil region. Their role is weighed by the value of χ, with ε^p_{12} increasing notably as χ decreases. The variations of γ_{12}, ε^p_{12}, and ϑ^p_{12} can be better appreciated in Fig. 4, where they are plotted as functions of the foil axis x_1.

As it can be seen in Fig. 4, in all cases γ_{12}, ε^p_{12}, and ϑ^p_{12} are monotonic functions of x_1, reaching the maximum at the foil end. Again, we observe that the contribution of ϑ^p_{12} to γ_{12} becomes dominant as χ decreases towards zero. Regarding $\varepsilon^p_{12}(x_1)$ one must note that there is a notable decrease in its slope for $x_1 \to W/2$. This is a consequence of the homogeneous microfree boundary conditions, requiring $\varepsilon_{12,1} = 0$ at $x_1 = W/2$ (see Eq. (38)). The peculiar development of γ_{12} at the foil end is due to the need of accommodating $\varepsilon^p_{11,2}$, as expressed by Eq. (37). In this region, when κ is large enough ε^p_{11} strongly varies with x_1, as shown in Fig. 5. Here, contrary to conventional plasticity, $|\varepsilon^p_{11,2}|$ increases with $|x_1|$.

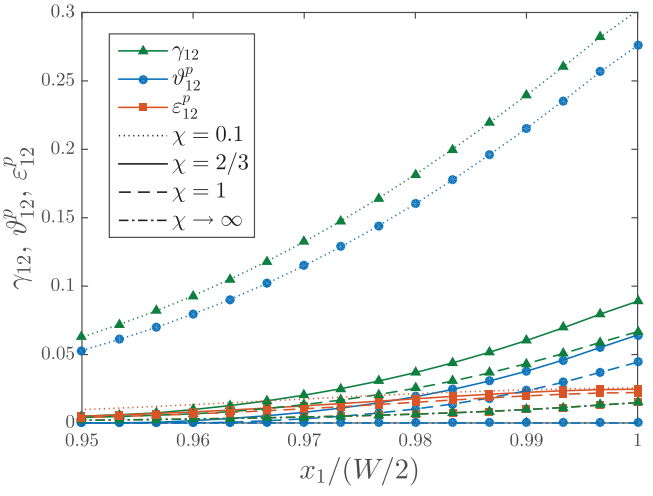

Fig. 4. Variation of γ_{12}, ε^p_{12}, and ϑ^p_{12} along x_1 ($x_2 = 0$) at $H\kappa/\sqrt{3} = 0.05$ for $\chi = 0.1$, 2/3, 1, and $\chi \to \infty$. The rate sensitivity exponent is $m = 0.05$.

The behavior so far described leads to a bending response dependent on the foil length W, for a given H. This can be seen clearly in Fig. 6, where the bending moment M is plotted versus the applied curvature for $W/H = 30$, $W/H = 60$, and $W/H = 120$.

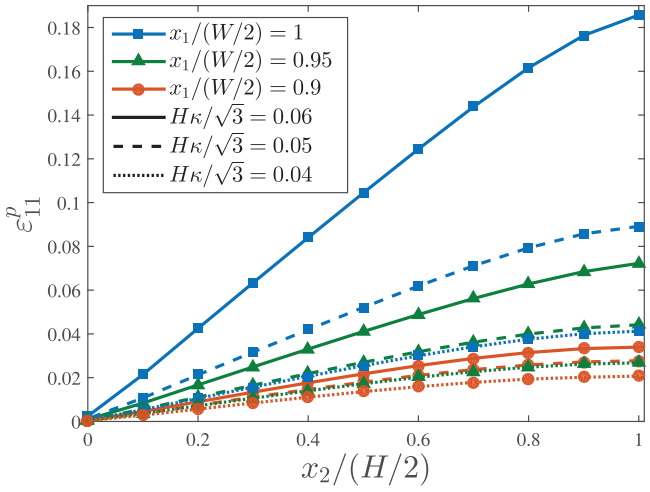

Fig. 5. Variation of ε^p_{11} along x_2 in different foil cross-sections at different applied curvature values. The following material properties are adopted: $\chi = 2/3$ and $m = 0.05$.

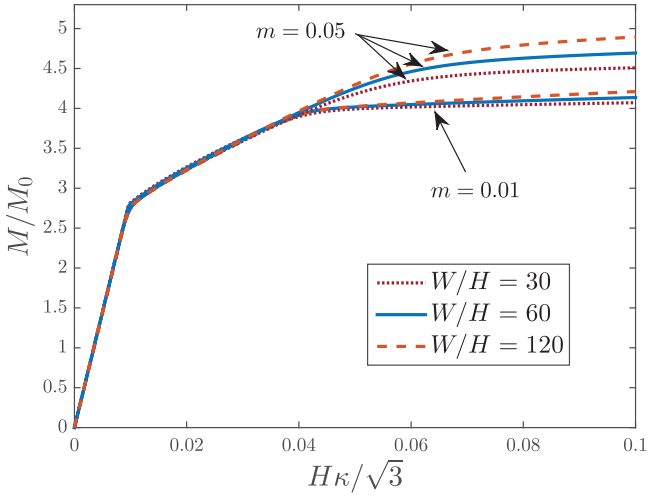

Fig. 6. Normalized moment versus curvature for different foil lengths with $\chi = 2/3$.

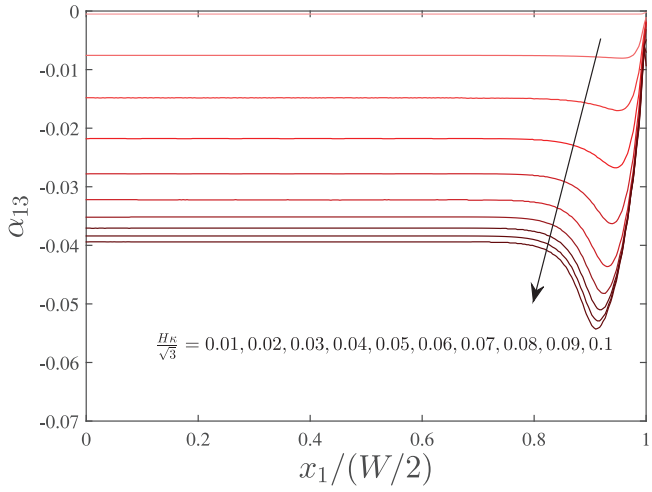

Fig. 7. Variation of α_{13} along x_1 (at $x_2 = H/4$) for $W/H = 30$ at different applied curvature values. The following material properties are adopted: $\chi = 2/3$ and $m = 0.05$.

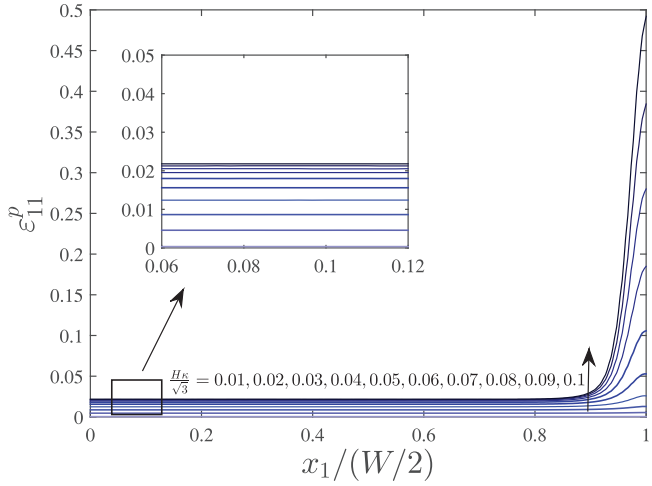

Fig. 8. Variation of ε^p_{11} along x_1 (at $x_2 = H/4$) for $W/H = 30$ at different applied curvature values. The following material properties are adopted: $\chi = 2/3$ and $m = 0.05$.

We consider two values of m to investigate the response by gradually approaching rate-independence. Here and henceforth, M is normalized by $M_0 = \sigma_0 H^2/(6\sqrt{1-\nu+\nu^2})$, defining initial yielding in conventional rate-independent, von Mises plasticity.

The response is more compliant as W diminishes, this behavior becoming irrelevant when the rate effects are small. After the initial elastic regime, delayed plasticity initiates at about $M/M_0 \approx 2.8$ as a consequence of the dissipative gradient effects. A hardening regime follows due to the build-up of free energy associated with Nye's tensor until the response eventually saturates. The asymptotic values of M are given by the minimizing field of functional (23) under the constraint $\dot{\boldsymbol{\alpha}} = \mathbf{0}$. As shown in Fig. 7, for large enough κ Nye's tensor becomes insensitive to further increase of κ.

More insight can be gained by inspection of the first scalar equation included in the tensorial higher-order balance equation (4), whose leading terms are:

$$\frac{\Sigma}{\dot{E}^p}\dot{\varepsilon}^p_{11} - \sigma_{11} + \frac{1}{2}\sigma_{33} + \mu\ell^2 \underbrace{(\gamma_{12,1} - \varepsilon^p_{11,2})_{,2}}_{\alpha_{13}} \approx 0 \tag{40}$$

where σ_{33} basically depends on σ_{11} through the hindered contraction along the x_3 direction, and we have neglected the terms $(\varepsilon^p_{22,1} - \gamma_{21,2})_{,1}$, $\varepsilon^p_{33,22}$, and $\varepsilon^p_{33,11}$. As already demonstrated, a quite large γ_{12} must develop at the foil end to satisfy condition $\alpha_{13} = 0$. At a certain level of κ, it may become energetically convenient for the model to accommodate further increments $\dot{u}_1$ by developing almost only ε^p_{11} in the foil end region, where γ_{12} is already conspicuous and may further develop in such a way as to make $\dot{\alpha}_{13} \approx 0$ pointwise in that domain. Thus, continued plastic deformation while preserving a constant Nye's tensor field leads to confinement of deformation close to the foil edge. In fact, examination of Eqs. (33)–(39) reveals that a constant Nye's tensor field hinders a one-dimensional structure of the solution. Let us emphasize that, under the boundary conditions here concerned, this behavior is not observed in GP theories whose primal higher-order kinematic variables just consist of the plain gradient of $\boldsymbol{\gamma}$ (or $\boldsymbol{\varepsilon}^p$) and its rate. In fact, in such GP theories the bending solution is in terms of the direct plastic strain components only, which turn out to be independent of x_1.

Fig. 8 displays $\varepsilon^p_{11}(x_1, x_2 = H/4)$ for various κ. It is observed that after a certain value of κ is reached, further increasing it leads to concentration of ε^p_{11} in the foil end region.

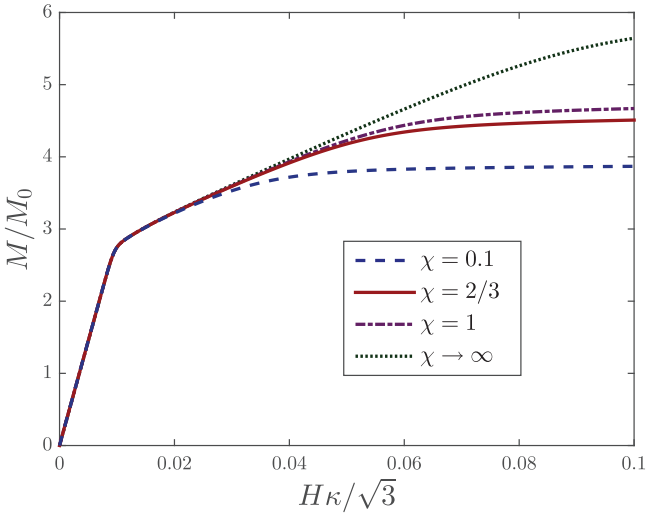

Fig. 9. Normalized moment versus curvature for different values of χ with $m = 0.05$.

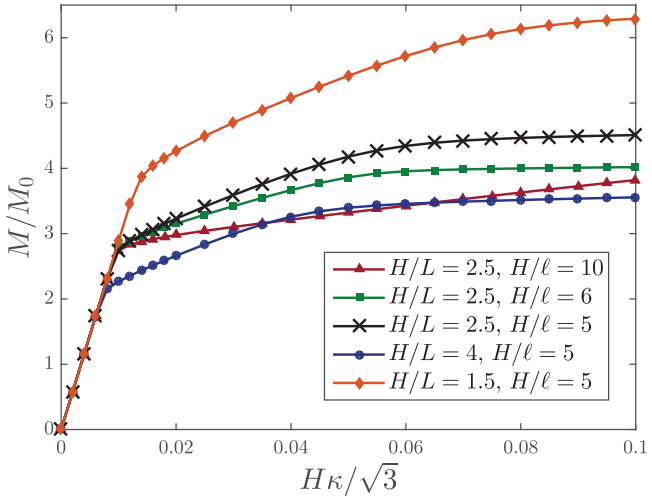

Fig. 10. Normalized moment versus curvature for different values of L and ℓ. Other material parameters are: $\chi = 2/3$ and $m = 0.05$.

This behavior is particularly favorable in the rate-independent case without isotropic hardening ($N = 0$) and implies no further appreciable increase of longitudinal elastic strain, in turn leading to vanishing increments of M. Under these circumstances, *since the foil end regions where γ_{12} significantly develops is proportional to the foil height H, not to the foil length W*, longer foils are subject to larger plastic flow at the foil end, for a given *applied curvature* κ. In fact, as evident from Eq. (31), for a given κ the *applied displacement* u_1 is proportional to W, whereas, in the picture above, u_1 is then distributed in the field ε^p_{11} solely over the foil end region.

Instead, if either rate-dependence or isotropic hardening are accounted for, Σ in the first term of relation (40) increases with plasticity, so that, if the behavior above described is still energetically convenient, such that the fourth term of (40) remains small, there is the need of an increase of the Cauchy stress to satisfy the higher-order balance equation. This makes M larger and leads to the observed behavior that *shorter foils have softer mechanical response* in the viscoplastic (or isotropic hardening) case. In fact, because of the above described way to develop plasticity, shorter the foil, at a given κ, lower $\dot{E}^p$ due to a further increase in κ. Hence, for a shorter foil there is less hardening in the M vs κ response. Consequently, γ_{12} in the foil end region increases with W for a given κ and the plastic spin may play a major role in slender foils (e.g., $W/H = 120$ as in the experimental work of Stölken and Evans, 1998). Let us finally remark that this behavior is the result of the *unique* solution of the analyzed micro-bending problem, so that it is unrelated to any *localization* phenomenon. Also, we remain agnostic on whether this behavior describes what really occurs at microfree boundaries subject to a direct plastic strain component, normal to the boundary, having a non-vanishing gradient along a tangential direction. Hopefully, in the future, new experiments will shed light on this.[4]

4.2. Influence of the unconventional material parameters on the micro-bending response

The influence of χ in the mechanical response is examined for the reference ratio $W/H = 30$ and results are reported in Fig. 9.

[4] Unfortunately, further insight may not be gained by comparing our predictions with the crystal plasticity predictions of Yefimov et al. (2004) and Yefimov and Giessen (2005), as in these works the foil edge regions are constrained to remain linear elastic at any curvature level.

It is observed that increasing χ promotes hardening in later deformation stages. More specifically, inspection of the higher-order balance equations (4) and (5) shows that augmenting χ, while penalizing the plastic spin, leads to a larger defect stress, which plays the role of a backstress in Eqs. (4) and (5) interpreted as a flow rule (Gurtin, 2004). Hence, the increase in hardening with χ shown in Fig. 9 actually consists of an increase in the kinematic hardening related to GNDs.

The role of the dissipative and energetic length scales in the M vs κ response has also been studied, as shown in Fig. 10. As expected, the dissipative length scale L governs the strengthening size effect: increasing L leads to a clear rise in what is recognized as the "initial yield moment". It can also be appreciated that the energetic length scale ℓ governs the increase in the (kinematic) strain hardening with diminishing size. Therefore, the foregoing results show that, by accounting for both energetic and dissipative higher-order contributions in Gurtin (2004) DGP theory, the present FE implementation can qualitatively reproduce the size effects observed in the experiments.

4.3. Mechanical response under non-proportional loading

Non-incremental dissipative higher-order terms (as referred to with the terminology used by Fleck et al., 2014) were introduced by Gurtin (2004) (see also Gudmundson, 2004; Gurtin and Anand, 2005) in such a way as to ensure that stresses associated with unrecoverable plastic flow always result in positive plastic work, as stated by Eq. (21) in the DGP here concerned. However, it has been very recently noticed (Fleck et al., 2014; 2015) that this may lead to a delay in plastic flow under certain non-proportional loading conditions, such a delay being referenced to as *elastic gap* by Fleck et al. (2014).

The boundary value problem under study is characterized by imposing microhard boundary conditions at the foil top and bottom surfaces after a significant amount of plasticity has developed in bending under microfree boundary conditions. Such a switch of higher-order boundary conditions models the formation of passivation layers. A perfectly plastic foil of ratio $W/H = 30$ is examined and the following material properties are adopted: $H/\ell = 5$, $\chi = 2/3$, $\sigma_0 = 200$ MPa, $\dot{\varepsilon}_0 = 0.02\ \text{s}^{-1}$, $m = 0.05$, $\nu = 0.3$, and $\mu = 26.3$ GPa. In general, dislocations are forced to pile-up at the boundary by imposing the microhard boundary conditions (8) or (9), depending on whether $L > 0$ or $L = 0$, respectively. Here, we impose microhard conditions (8) because the case without dissipative higher-

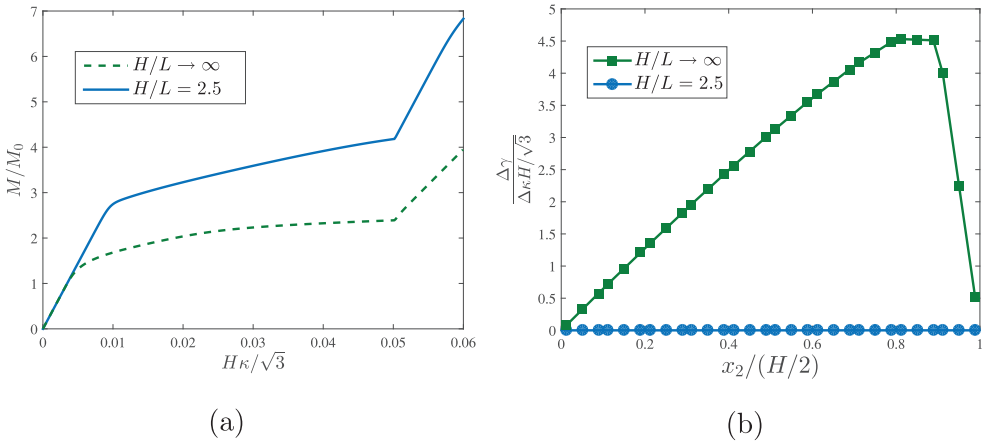

Fig. 11. Effect of the application of a passivation layer: (a) Normalized moment versus curvature for different values of L and (b) normalized plastic distortion increments along the thickness of the foil immediately after passivation. Other material parameters are $\chi = 2/3$ and $m = 0.05$.

order effect, $H/L \to \infty$, is numerically treated by choosing an appropriately small positive value for L. Finally, the microhard conditions (8), in the plane strain case here of interest, turn out to imply

$$\dot{\boldsymbol{\gamma}} = \mathbf{0} \quad \text{at} \quad x_2 = \pm H/2 \tag{41}$$

Results obtained after switching the higher-order boundary conditions at $H\kappa/\sqrt{3} \approx 0.05$ are displayed in Fig. 11, which clearly shows an abrupt stiffening at the formation of the passivation layers.

Qualitatively, the two options examined ($L \to 0$ or $L > 0$) seem to lead to totally similar M vs κ responses. However, the two mechanical behaviors are very different, as observable in Fig. 11b, showing the incremental plastic distortion along the thickness of the mid-section ($x_1 = 0$) immediately after passivation. Here, the incremental plastic distortion is represented in terms of its modulus $\Delta\gamma = \Delta t|\dot{\boldsymbol{\gamma}}|$, with Δt the time increment, and it is normalized by $\Delta\kappa = \Delta t\ \dot{\kappa}$.

Results reveal that setting $L > 0$ leads to a purely elastic incremental response after formation of the passivation layer. This elastic gap after switching higher-order boundary conditions has been also numerically observed by Bardella and Panteghini (2015) in the torsion problem governed by DGP. As shown in Fig. 11b, the elastic gap may be avoided by suppressing the unrecoverable higher-order term (i.e., by setting $L \to 0$). Our results provide further numerical evidence of the analytical findings of Fleck et al. (2014). This may favor the "incremental" modeling approach suggested by Hutchinson (2012), where incremental relations between all the stress and strain variables are employed. Nevertheless, one should note that for $L \to 0$ the present formulation still has finite unrecoverable stresses constitutively conjugate to the plastic distortion rate, but not its gradient, which is the key issue pointed out by Fleck et al. (2014; 2015).

5. Concluding remarks

In small-scale plasticity, the superior modeling capabilities associated with the constitutive inclusion of the plastic spin has recently encouraged significant interest in *Distortion Gradient Plasticity* (DGP). In this work, we present a novel general purpose Finite Element (FE) framework for gradient theories involving the plastic spin, that is the skew-symmetric part of the plastic distortion. The proposed FE framework rests on two extremum principles and allows for an accurate modeling of both viscoplastic and rate-independent material responses. Such extremum principles extend to DGP those established by Fleck and Willis (2009b) for Strain Gradient Plasticity (SGP).

More specifically, we have focused on Gurtin (2004) DGP, which is characterized by the choice of Nye's dislocation density tensor as primal higher-order kinematic variable, leading to a higher-order energetic stress, called defect stress, increasing with the plastic distortion incompatibility and governed by an energetic material length scale.

We have employed the novel FE framework for Gurtin (2004) DGP to implement general purpose plane strain elements. The new numerical algorithm has been first validated against literature results on the simple shear of a strip constrained between bodies impenetrable to dislocations.

Second, some specific features of Gurtin (2004) DGP theory have been analyzed by studying the bending of thin metal foils. Results show a strong influence of one shear component of the plastic distortion under microfree and conventional pure bending boundary conditions: we have illustrated in detail the development of relevant plastic shear strain and spin required to compensate for the variation along the foil thickness of the longitudinal plastic strain. This peculiarity is due to the form assumed by the microfree boundary conditions in higher-order gradient plasticity based on Nye's tensor.

For a given foil thickness, this feature turns out in a mechanical response exhibiting dependence on the foil length, with shorter foils being softer, if either rate-dependence or isotropic hardening are included in the modeling. This behavior is also due to the imposed foil ends rotations, that are governed by the application of an average foil curvature.

The peculiar mechanism observed not only reveals a major role of the plastic spin but also indicates that analogous issues may be inherent to strain gradient *crystal* plasticity theories involving Nye's dislocation density tensor as primal higher-order kinematic variable. In this context, counterintuitive coupling effects among slip systems have already been observed by Bardella et al. (2013).

The micro-bending benchmark has also been employed to investigate the existence of "elastic gaps" under non-proportional loading, as recently defined by Fleck et al. (2014). The proposed FE framework can predict that, in the present "non-incremental" DGP theory, a purely elastic incremental response follows passivation in the plastic regime. Critical experiments are needed to gain insight into the existence, or lack thereof, of the interruptions in plastic flow due to specific non-proportional loading conditions. Nevertheless, our FE analysis confirms that by assuming a vanishing value for the dissipative length scale governing the dissipative higher-order stress, the present DGP formulation is free from such "elastic gaps".

Acknowledgments

Dr. Andrea Panteghini and Prof. Samuel Forest are acknowledged for helpful discussions. The authors gratefully acknowledge financial support from the Danish Council for Independent Research under the research career programme Sapere Aude in the project "Higher Order Theories in Solid Mechanics". E. Martínez-Pañeda also acknowledges financial support from the Ministry of Science and Innovation of Spain through grant MAT2011-28796-CO3-03, and the University of Oviedo through grant UNOV-13-PF and an excellence mobility grant within the International Campus of Excellence programme. L. Bardella additionally acknowledges financial support from the Italian Ministry of Education, University, and Research (MIUR).

Appendix A. Matrix operators for the discretization of the plastic variables

The following matrices are defined in such a way as when they are multiplied by the column vector containing the four plastic distortion components of a node, say $[\gamma_{11}^{(i)},\ \gamma_{22}^{(i)},\ \gamma_{12}^{(i)},\ \gamma_{21}^{(i)}]^T$, they deliver its contribution to the vector fields containing the relevant components of the plastic strain $[\varepsilon_{11}^{p(i)},\ \varepsilon_{22}^{p(i)},\ \varepsilon_{12}^{p(i)},\ \varepsilon_{21}^{p(i)},\ \varepsilon_{33}^{p(i)}]^T$, the plastic spin $[\vartheta_{12}^{p(i)},\ \vartheta_{21}^{p(i)}]^T$, the gradient of the plastic strain $[\varepsilon_{11,1}^{p(i)},\ \varepsilon_{11,2}^{p(i)},\ \varepsilon_{22,1}^{p(i)},\ \varepsilon_{22,2}^{p(i)},\ \varepsilon_{12,1}^{p(i)},\ \varepsilon_{12,2}^{p(i)}\varepsilon_{21,1}^{p(i)},\ \varepsilon_{21,2}^{p(i)},\ \varepsilon_{33,1}^{p(i)},\ \varepsilon_{33,2}^{p(i)}]^T$, and Nye's tensor $[\alpha_{13}^{(i)},\ \alpha_{23}^{(i)},\ \alpha_{31}^{(i)},\ \alpha_{32}^{(i)}]^T$, respectively:

$$\operatorname{sym}\boldsymbol{M}^{(i)} = \begin{bmatrix} N_i & 0 & 0 & 0 \\ 0 & N_i & 0 & 0 \\ 0 & 0 & \frac{1}{2}N_i & \frac{1}{2}N_i \\ 0 & 0 & \frac{1}{2}N_i & \frac{1}{2}N_i \\ -N_i & -N_i & 0 & 0 \end{bmatrix} \tag{A.1}$$

$$\operatorname{skw}\boldsymbol{M}^{(i)} = \begin{bmatrix} 0 & 0 & \frac{1}{2}N_i & -\frac{1}{2}N_i \\ 0 & 0 & -\frac{1}{2}N_i & \frac{1}{2}N_i \end{bmatrix} \tag{A.2}$$

$$\operatorname{sym}\nabla\boldsymbol{M}^{(i)} = \begin{bmatrix} \frac{\partial N_i}{\partial x} & 0 & 0 & 0 \\ \frac{\partial N_i}{\partial y} & 0 & 0 & 0 \\ 0 & \frac{\partial N_i}{\partial x} & 0 & 0 \\ 0 & \frac{\partial N_i}{\partial y} & 0 & 0 \\ 0 & 0 & \frac{1}{2}\frac{\partial N_i}{\partial x} & \frac{1}{2}\frac{\partial N_i}{\partial x} \\ 0 & 0 & \frac{1}{2}\frac{\partial N_i}{\partial y} & \frac{1}{2}\frac{\partial N_i}{\partial y} \\ 0 & 0 & \frac{1}{2}\frac{\partial N_i}{\partial x} & \frac{1}{2}\frac{\partial N_i}{\partial x} \\ 0 & 0 & \frac{1}{2}\frac{\partial N_i}{\partial y} & \frac{1}{2}\frac{\partial N_i}{\partial y} \\ -\frac{\partial N_i}{\partial x} & -\frac{\partial N_i}{\partial x} & 0 & 0 \\ -\frac{\partial N_i}{\partial y} & -\frac{\partial N_i}{\partial y} & 0 & 0 \end{bmatrix} \tag{A.3}$$

$$\operatorname{curl}\boldsymbol{M}^{(i)} = \begin{bmatrix} -\frac{\partial N_i}{\partial y} & 0 & \frac{\partial N_i}{\partial x} & 0 \\ 0 & \frac{\partial N_i}{\partial x} & 0 & -\frac{\partial N_i}{\partial y} \\ -\frac{\partial N_i}{\partial y} & -\frac{\partial N_i}{\partial y} & 0 & 0 \\ \frac{\partial N_i}{\partial x} & -\frac{\partial N_i}{\partial x} & 0 & 0 \end{bmatrix} \tag{A.4}$$

References

Arsenlis, A., Parks, D.M., 1999. Crystallographic aspects of geometrically-necessary and statistically-stored dislocation density. Acta Mater. 47, 1597–1611.
Ashby, M.F., 1970. The deformation of plastically non-homogeneous materials. Philos. Mag. 21, 399–424.
Bardella, L., 2009. A comparison between crystal and isotropic strain gradient plasticity theories with accent on the role of the plastic spin. Eur. J. Mech. A. Solids 28, 638–646.
Bardella, L., 2010. Size effects in phenomenological strain gradient plasticity constitutively involving the plastic spin. Int. J. Eng. Sci. 48, 550–568.
Bardella, L., Giacomini, A., 2008. Influence of material parameters and crystallography on the size effects describable by means of strain gradient plasticity. J. Mech. Phys. Solids 56, 2906–2934.
Bardella, L., Panteghini, A., 2015. Modelling the torsion of thin metal wires by distortion gradient plasticity. J. Mech. Phys. Solids 78, 467–492.
Bardella, L., Segurado, J., Panteghini, A., Llorca, J., 2013. Latent hardening size effect in small-scale plasticity. Modell. Simul. Mater. Sci. Eng. 21, 055009.
Bittencourt, E., Needleman, A., Gurtin, M.E., Van der Giessen, E., 2003. A comparison of nonlocal continuum and discrete dislocation plasticity predictions. J. Mech. Phys. Solids 51, 281–310.
Borg, U., Niordson, C.F., Fleck, N.A., Tvergaard, V., 2006. A viscoplastic strain gradient analysis of materials with voids or inclusions. Int. J. Solids Struct. 43, 4906–4916.
Engelen, R.A.B., Fleck, N.A., Peerlings, R.H.J., Geers, M.G.D., 2006. An evaluation of higher-order plasticity theories for predicting size effects and localisation. Int. J. Solids Struct. 43, 1857–1877.
Evans, A.G., Hutchinson, J.W., 2009. A critical assessment of theories of strain gradient plasticity. Acta Mater. 57, 1675–1688.
Fleck, N.A., Hutchinson, J.W., 1997. Strain gradient plasticity. Adv. Appl. Mech. 33, 295–361.
Fleck, N.A., Hutchinson, J.W., 2001. A reformulation of strain gradient plasticity. J. Mech. Phys. Solids 41, 1825–1857.
Fleck, N.A., Hutchinson, J.W., Willis, J.R., 2014. Strain gradient plasticity under non–proportional loading. Proc. R. Soc. London, Ser. A 470, 20140267.
Fleck, N.A., Hutchinson, J.W., Willis, J.R., 2015. Guidelines for Constructing Strain Gradient Plasticity Theories. J. Appl. Mech. 82 (071002), 1–10.
Fleck, N.A., Muller, G.M., Ashby, M.F., Hutchinson, J.W., 1994. Strain gradient plasticity: theory and experiment. Acta Metall. Mater. 42, 475–487.
Fleck, N.A., Willis, J.R., 2009a. A mathematical basis for strain-gradient plasticity theory - part i: Scalar plastic multiplier. J. Mech. Phys. Solids 57, 161–177.
Fleck, N.A., Willis, J.R., 2009b. A mathematical basis for strain-gradient plasticity theory - part II: tensorial plastic multiplier. J. Mech. Phys. Solids 57, 1045–1057.
Forest, S., Guéninchault, N., 2013. Inspection of free energy functions in gradient crystal plasticity. Acta Mech. Sin. 29, 763–772.
Fredriksson, P., Gudmundson, P., 2005. Size-dependent yield strength of thin films. Int. J. Plast. 21, 1834–1854.
Gao, H., Huang, Y., Nix, W.D., Hutchinson, J.W., 1999. Mechanism-based strain gradient plasticity i. theory. J. Mech. Phys. Solids 47, 1239–1263.
Garroni, A., Leoni, G., Ponsiglione, M., 2010. Gradient theory for plasticity via homogenization of discrete dislocations. J. Eur. Math. Soc. 12, 1231–1266.
Gudmundson, P., 2004. A unified treatment of strain gradient plasticity. J. Mech. Phys. Solids 52, 1379–1406.
Gurtin, M.E., 2004. A gradient theory of small-deformation isotropic plasticity that accounts for the burgers vector and for dissipation due to plastic spin. J. Mech. Phys. Solids 52, 2545–2568.
Gurtin, M.E., Anand, L., 2005. A theory of strain-gradient plasticity for isotropic, plastically irrotational materials. part i: small deformations. J. Mech. Phys. Solids 53, 1624–1649.
Gurtin, M.E., Anand, L., 2009. Thermodynamics applied to gradient theories involving the accumulated plastic strain: The theories of aifantis and fleck & hutchinson and their generalization. J. Mech. Phys. Solids 57, 405–421.
Gurtin, M.E., Needleman, A., 2005. Boundary conditions in small-deformation, single-crystal plasticity that account for the burgers vector. J. Mech. Phys. Solids 53, 1–31.
Hutchinson, J.W., 2012. Generalizing J_2 flow theory: fundamental issues in strain gradient plasticity. Acta Mech. Sin. 28, 1078–1086.
Idiart, M.I., Deshpande, V.S., Fleck, N.A., Willis, J.R., 2009. Size effects in the bending of thin films. Int. J. Eng. Sci. 47, 1251–1264.
Klusemann, B., Svendsen, B., Vehoff, H., 2013. Modeling and simulation of deformation behavior, orientation gradient development and heterogeneous hardening in thin sheets with coarse texture. Int. J. Plast. 50, 109–126.
Lancioni, G., Yalçinkaya, T., Cocks, A., 2015. Energy-based non-local plasticity models for deformation patterning, localization and fracture. Proc. R. Soc. London, Ser. A 471, 20150275.
Legarth, B.N., Niordson, C.F., 2010. Debonding failure and size effects in micro reinforced composites. Int. J. Plast. 26, 149–165.
Liu, B., Huang, Y., Li, M., Hwang, K.C., Liu, C., 2005. A study of the void size effect based on the taylor dislocation model. Int. J. Plast. 21, 2107–2122.
Martínez-Pañeda, E., Betegón, C., 2015. Modeling damage and fracture within strain gradient plasticity. Int. J. Solids Struct. 59, 208–215.
Martínez-Pañeda, E., Niordson, C.F., 2016. On fracture in finite strain gradient plasticity. Int. J. Plast. 80, 154–167.
Moreau, P., Raulic, M., P'ng, M.Y., Gannaway, G., Anderson, P., Gillin, W.P., Bushby, A.J., Dunstan, D.J., 2005. Measurement of the size effect in the yield strength of nickel foils. Philos. Mag. Lett. 85, 339–343.
Nielsen, K.L., Niordson, C.F., 2014. A numerical basis for strain-gradient plasticity theory: Rate-independent and rate-dependent formulations. J. Mech. Phys. Solids 63, 113–127.
Niordson, C.F., 2003. Strain gradient plasticity effects in whisker-reinforced metals. J. Mech. Phys. Solids 51, 1863–1883.

Niordson, C.F., 2007. Size-effects in porous metals. Modell. Simul. Mater. Sci. Eng. 15, 51–60.
Niordson, C.F., Hutchinson, J.W., 2011. Basic strain gradient plasticity theories with application to constrained film deformation. J. Mech. Mater. Struct. 6, 395–416.
Niordson, C.F., Legarth, B.N., 2010. Strain gradient effects on cyclic plasticity. J. Mech. Phys. Solids 58, 542–557.
Nix, W.D., Gao, H., 1998. Indentation size effects in crystalline materials: a law for strain gradient plasticity. J. Mech. Phys. Solids 46, 411–425.
Nye, J.F., 1953. Some geometrical relations in dislocated crystals. Acta Metall. 1, 153–162.
Ohno, N., Okumura, D., 2007. Higher-order stress and grain size effects due to self-energy of geometrically necessary dislocations. J. Mech. Phys. Solids 55, 1879–1898.
Ostien, J., Garikipati, K., 2008. Galerkin method for an incompatibility-based strain gradient plasticity theory. In: IUTAM Symposium on Theoretical, Computational and Modelling Aspects of Inelastic Media. Springer, Netherlands, pp. 217–226.
Poh, L.H., 2013. Scale transition of a higher order plasticity model - a consistent homogenization theory from meso to macro. J. Mech. Phys. Solids 61, 2692–2710.
Poh, L.H., Peerlings, R.H.J., 2016. The plastic rotation effect in an isotropic gradient plasticity model for applications at the meso scale. Int. J. Solids Struct. 78–79, 57–69.
Poh, L.H., Phan, V.T., 2016. Numerical implementation and validation of a consistently homogenized higher order plasticity model. Int. J. Numer. Methods Eng. 106, 454–483.
Polizzotto, C., 2011. Size effects on the plastic collapse limit load of thin foils in bending and thin wires in torsion. Eur. J. Mech. A. Solids 30, 854–864.
Qu, S., Huang, Y., Pharr, G.M., Hwang, K.C., 2006. The indentation size effect in the spherical indentation of iridium: a study via the conventional theory of mechanism-based strain gradient plasticity. Int. J. Plast. 22, 1265–1286.
Stölken, J.S., Evans, A.G., 1998. A microbend test method for measuring the plasticity length scale. Acta Mater. 46, 5109–5115.
Wieners, C., Wohlmuth, B., 2011. A primal-dual finite element approximation for a nonlocal model in plasticity. SIAM J. Numer. Anal. 49, 692–710.
Yefimov, S., Van der Giessen, E., 2005. Multiple slip in a strain-gradient plasticity model motivated by a statistical-mechanics description of dislocations. Int. J. Solids Struct. 42, 3375–3394.
Yefimov, S., Van der Giessen, E., Groma, I., 2004. Bending of a single crystal: discrete dislocation and nonlocal crystal plasticity simulations. Modelling Simul. Mater. Sci. Eng. 12, 1069–1086.